ADVANCED SUSTAINABLE SYSTEMS
www.advsustainsys.com

High Performance Nonaqueous Ca-Ion Cathodes Based on NASICON-$NaV_2(PO_4)_3$ and the Way to Activate Their Structure

Hyungjin Lee, Jangwook Pyun, Yeonu Lee, Hyeonjun Lee, Seung-Tae Hong, and Munseok S. Chae**

Calcium-ion batteries (CIBs) are gaining attention as a promising energy storage technology due to their high theoretical capacity, attributed to the divalency of calcium, low redox potential, and natural abundance. However, the limited availability of calcium insertion electrode materials and their tendency to exhibit low capacity or poor cyclability remain critical challenges. In this study, the activation mechanism underlying calcium ion storage in NASICON-type $NaV_2(PO_4)_3$ structures are investigated using advanced structural analyses and elemental analyses. $NaV_2(PO_4)_3$ is identified as an efficient cathode material for CIBs, demonstrating a reversible discharge capacity of 106.9 mAh g^{-1} at 10 mA g^{-1}—an 82% improvement compared to the pristine material—while maintaining an average operating voltage of ≈3.5 V (vs Ca/Ca^{2+}) and good cyclability in a nonaqueous electrolyte. These findings offer valuable insights into the design and development of advanced oxide-based cathodes, enhancing their performance through activation processes for nonaqueous CIBs.

1. Introduction

The pursuit of rechargeable batteries with enhanced energy density and cost efficiency compared to traditional lithium-ion batteries (LIBs) drives ongoing research into post-LIB technologies.[1] Among the most promising alternatives are multivalent-ion batteries, which utilize divalent or trivalent ions (e.g., Mg^{2+}, Ca^{2+}, Zn^{2+}, Al^{3+}) and offer the potential to surpass the energy density limitations of LIBs.[2–6] In particular, calcium-ion batteries (CIBs) have garnered significant attention, driven by recent advancements in anode technology. Reversible calcium plating and stripping have been successfully demonstrated at both elevated temperatures (75–100 °C) and room temperature.[7,8] Additionally, calcium alloying with tin anodes and calcium intercalation into graphite have been reported, further advancing the feasibility of CIBs.[9,10]

The divalent nature of calcium theoretically enables host materials to achieve double the capacity, as each calcium ion facilitates the transfer of two electrons, provided the host's transition metal can accommodate the additional charge. Moreover, calcium's abundance in Earth's crust presents significant cost advantages for battery production.[11,12] With a redox potential of −2.87 V vs SHE, close to that of lithium, calcium allows for high cell voltages. Its low effective intercalant-ion charge density (0.49 e $Å^{-3}$) compared to other divalent cations such as Mg^{2+} (1.28 e $Å^{-3}$) and Zn^{2+} (1.18 $e^{-}Å^{3}$) further enhances diffusion kinetics in solid-state materials and electrolytes.[4]

Despite these advantages, translating recent breakthroughs in anode and electrolyte development into viable full-cell calcium-ion batteries has been challenging. Issues such as low Coulombic efficiencies and unwanted side reactions have hindered progress.[13,14] Nevertheless, these advancements have catalyzed intensive research efforts aimed at identifying high-performance calcium-intercalating cathode materials. While computational studies have predicted several promising high-energy cathode candidates,[15,16] experimental validation has been limited. To date, only a few materials have been shown to electrochemically intercalate calcium ions in nonaqueous electrolytes, including α-V_2O_5,[17] $(NH_4)_2V_7O_{16}$,[18] $NH_4V_4O_{10}$,[19] α-MoO_3,[20] Ca_xMoO_3,[21] $Ca_{0.13}MoO_3{\cdot}(H_2O)_{0.41}$,[22] $CaCo_2O_4$,[23] TiS_2,[24–26] Na_2FePO_4F,[27] $FeV_3O_9{\bullet}1.2H_2O$,[28] $Mg_{0.25}V_2O_5{\cdot}H_2O$,[29] and some organic

H. Lee, Y. Lee, S.-T. Hong
Department of Energy Science and Engineering
DGIST
Daegu 42988, Republic of Korea
E-mail: st.hong@dgist.ac.kr
S.-T. Hong
Department of Chemistry and Chemical Biology
University of New Mexico
Albuquerque, New Mexico 87131, USA
J. Pyun, H. Lee, M. S. Chae
Department of Nanotechnology Engineering
Pukyong National University
Busan 48547, Republic of Korea
E-mail: mschae@pknu.ac.kr

The ORCID identification number(s) for the author(s) of this article can be found under https://doi.org/10.1002/adsu.202500585

DOI: 10.1002/adsu.202500585

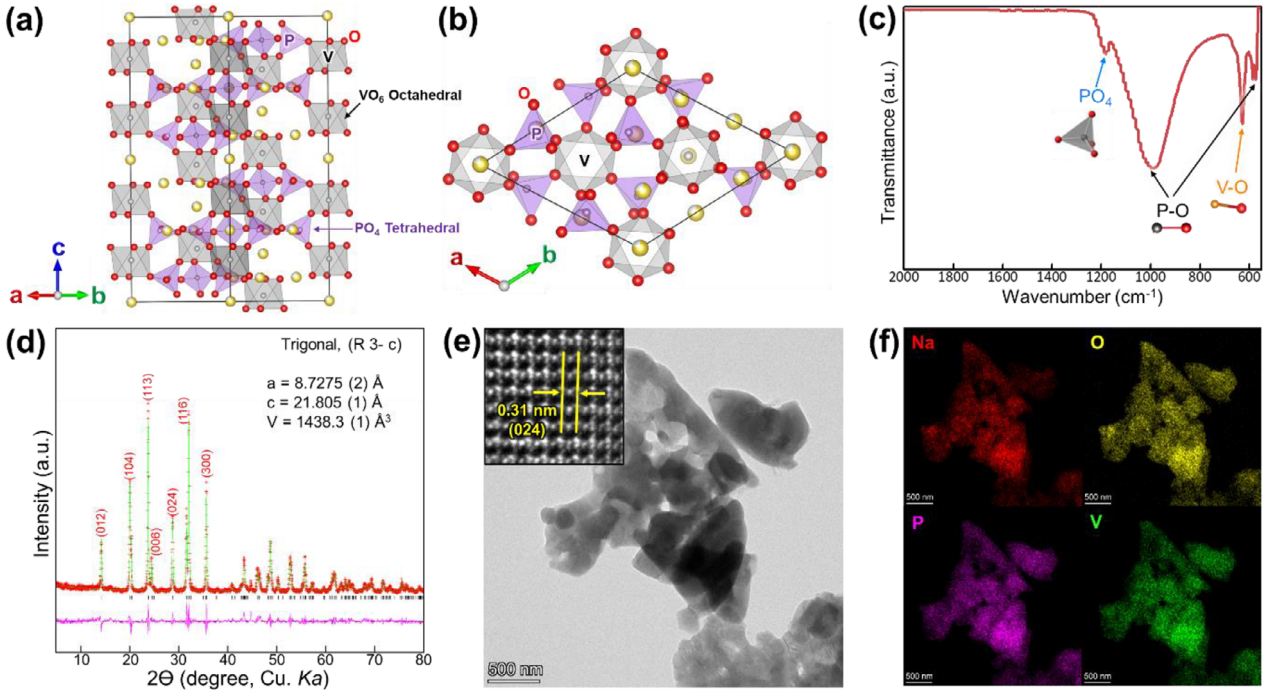

Figure 1. a) (101) view of the NASICON-$Na_3V_2(PO_4)_3$ structure, b) (010) view of the $Na_3V_2(PO_4)_3$ structure and local environment of PO_4 tetrahedra surrounded by four VO_6 octahedra, c) FTIR spectra of synthesized $Na_3V_2(PO_4)_3$ powder, d) Powder Rietveld refinement result of synthesized $Na_3V_2(PO_4)_3$, e) TEM images (inset: high-resolution lattice fringe), and f) TEM-EDX elemental mapping of sodium(red), oxygen(yellow), phosphorus(pink), and vanadium(green) of $Na_3V_2(PO_4)_3$ powder.

electrodes (PTCDA[30] Prussian-blue analogues[31–36]). However, these materials typically exhibit limitations such as low capacity, poor Coulombic efficiency, or limited cyclability. Moreover, some compounds require the presence of significant water content in organic electrolytes, which introduces complications like proton/hydronium intercalation or water-related side reactions that compromise practicality. Among the available cathode structures, the NASICON-type $NaV_2(PO_4)_3$ has demonstrated stable calcium storage capabilities in our previous studies.[37] However, its low electrochemical performance restricts its potential as a viable cathode material. To address these limitations, both electrolyte optimization and structural activation of NASICON materials are essential.

In this study, we investigate the activation mechanism governing calcium ion storage in the NASICON-type $NaV_2(PO_4)_3$ structure. We also introduce a highly stable calcium electrolyte composition, 1 M $Ca(BF_4)_2$ in EC:PC (Vol/Vol = 1:1), which enhances electrochemical performance. Ultimately, we demonstrate excellent calcium ion storage capabilities in $NaV_2(PO_4)_3$ at room temperature, achieving stable operation in the 3.0 V range. These findings position NASICON $NaV_2(PO_4)_3$ as a promising cathode material for nonaqueous calcium-ion batteries, advancing the field toward practical applications.

2. Results and Discussion

2.1. $Na_3V_2(PO_4)_3$ Synthesis and Characterization

The NASICON-type $Na_3V_2(PO_4)_3$ is characterized by an open three-dimensional framework composed of corner-shared PO_4 tetrahedra and VO_6 octahedra, as illustrated in **Figure 1**a,b. To prepare $NaV_2(PO_4)_3$, two sodium ions were extracted from carbon-coated $Na_3V_2(PO_4)_3$, which was synthesized using the sol–gel method (Figures S1–S3, Supporting Information).[37] Detailed synthesis protocols are provided in the experimental section. A comprehensive characterization of the synthesized material was conducted using Fourier-transform infrared spectroscopy (FTIR), X-ray diffraction (XRD), and transmission electron microscopy (TEM) coupled with energy-dispersive X-ray spectroscopy (EDX).

FTIR analysis (Figure 1c) identified distinct absorption bands characteristic of the material's chemical bonds: bands at 590 and 990 cm^{-1} were attributed to P—O stretching, a band at 940 cm^{-1} corresponded to V—O stretching, and a band at 1180 cm^{-1} was assigned to P—O_4 stretching vibrations. The powder XRD pattern, presented in Figure 1d, confirms the material's trigonal crystal structure belonging to the R $\bar{3}$ c space group. The refined lattice parameters were determined to be a = 8.7275(2) Å and c = 21.805(1) Å, consistent with previously reported values for similar NASICON-type compounds. Additional crystallographic details are provided in Table S1 (Supporting Information).

The morphology and nanostructure of the synthesized material were examined through TEM analysis. As shown in Figure 1e, $Na_3V_2(PO_4)_3$ particles exhibited a sub-micron size, with diameters averaging ≈700 nm. High-resolution TEM images (inset, Figure 1e) revealed well-defined crystalline lattice fringes, with a d(024) spacing of ≈0.31 nm, further confirming the material's crystalline nature. Elemental analysis was performed using TEM-EDS mapping, with the results presented in Figure 1f. The maps revealed a homogeneous distribution of

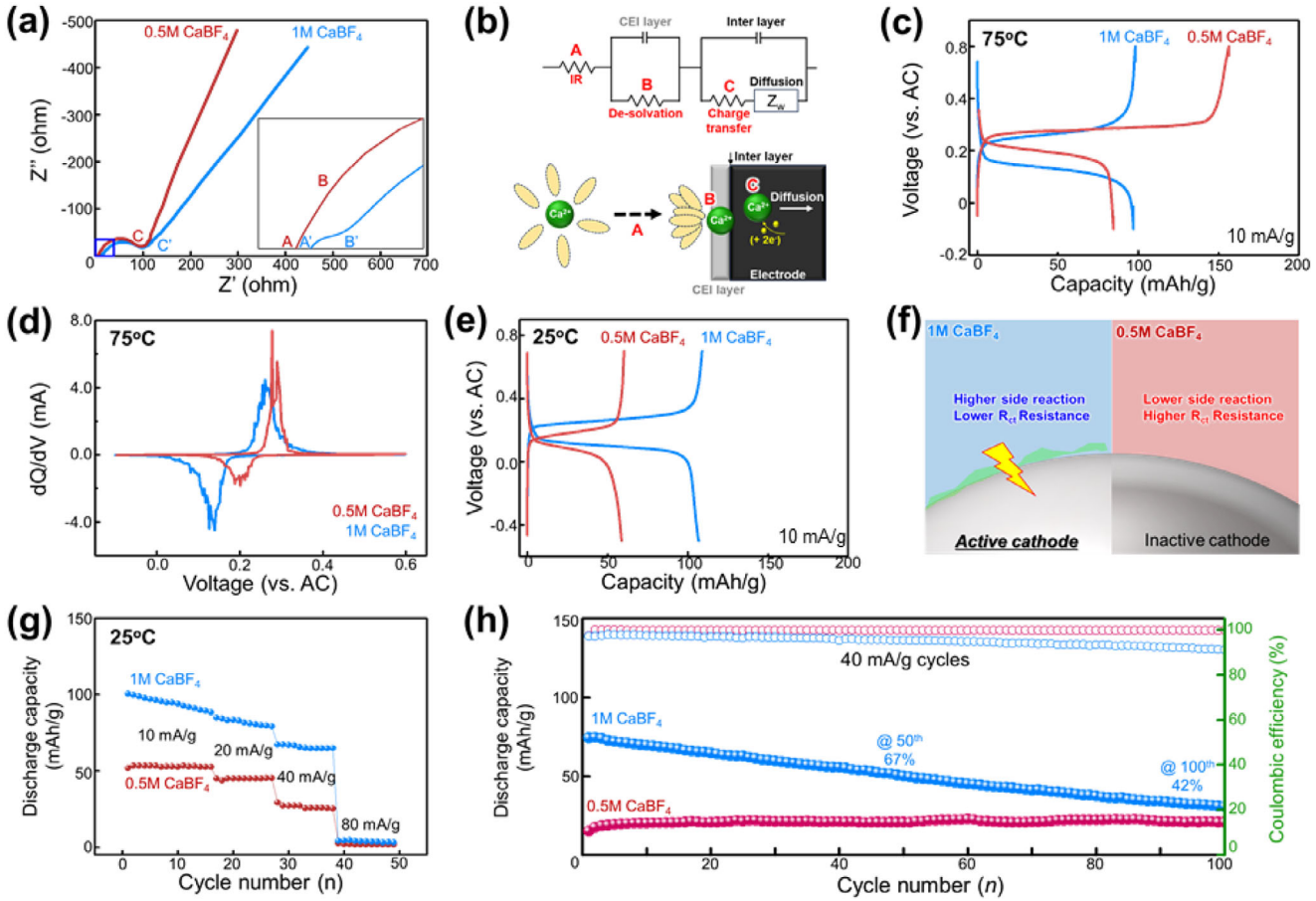

Figure 2. Electrochemical test of activated carbon/0.5 and 1 M $Ca(BF_4)_2$ in EC:PC (Vol/Vol = 1:1)/$Na_1V_2(PO_4)_3$ cell: a) impedance spectra, and their b) impedance circuit, c) galvanostatic charge/discharge of $Na_1V_2(PO_4)_3$ at 75 °C for activation process under 10 mA g^{-1} current, and d) dQ/dV graph at 75 °C, e) galvanostatic charge/discharge of $Na_1V_2(PO_4)_3$ at 25 °C under 10 mA g^{-1} current, f) schematic illustration of reaction mechanism between two different molar concentration electrolytes, g) rate capability, h) cyclability of each cells.

sodium (Na), oxygen (O), phosphorus (P), and vanadium (V) elements throughout the material. This uniformity in elemental distribution underscores the quality of the synthesis process and ensures stoichiometric consistency in the prepared $Na_3V_2(PO_4)_3$.

2.2. Electrochemical Calcium Storage Performance

All electrochemical measurements were conducted using a custom-made cell (Figure S2, Supporting Information). The $Na_1V_2(PO_4)_3$ phase was synthesized electrochemically by extracting sodium from $Na_3V_2(PO_4)_3$ via galvanostatic charging, as shown in Figure S3 (Supporting Information). Electrochemical impedance spectroscopy (EIS) was performed using an activated carbon/$Ca(BF_4)_2$ in EC:PC (Vol/Vol = 1:1)/ $Na_1V_2(PO_4)_3$ cell system (**Figure** 2a). The internal resistance (IR) at point A was lower in the 0.5 M $Ca(BF_4)_2$ electrolyte (6.95 Ω) compared to the 1.0 M $Ca(BF_4)_2$ electrolyte (8.19 Ω), indicating enhanced ionic conductivity at the lower concentration (Table S2, Supporting Information) because of viscosity. It should be noted that the accessible concentration window of $Ca(BF_4)_2$ in EC:PC (1:1, v/v) is limited between 0.5 and 1.0 M due to ionic conductivity and solubility constraints (Table S2, Supporting Information). Concentrations below 0.5 M exhibit insufficient conductivity, while attempts above 1.0 M lead to precipitation, thus restricting the systematic comparison to these two representative cases. At point B, the cathode electrolyte interphase (CEI) resistance—representing interfacial resistance caused by CEI formation—was markedly lower for the 0.5 M electrolyte (3.297 Ω) than for the 1.0 M electrolyte (14.4 Ω). In the highly concentrated electrolyte, the increased occurrence of side reactions leads to the formation of a relatively less stable interface than that formed in the low-concentration electrolyte, thereby contributing to the higher interfacial resistance. Point C corresponds to the charge-transfer resistance, recorded at 91.19 Ω for the 0.5 M electrolyte and 70.8 Ω for the 1.0 M electrolyte, indicating a decrease in resistance with increasing concentration. This decrease is attributed to enhanced interfacial reaction kinetics resulting from a higher concentration of mobile ions, which subsequently facilitates the activation process described in the following section. A significant difference was noted in the Warburg impedance, as reflected by the slope in the low-frequency region. The 0.5 M $Ca(BF_4)_2$ electrolyte exhibited a steeper Warburg slope, implying improved Ca^{2+} diffusion kinetics within the electrode matrix. The equivalent circuit

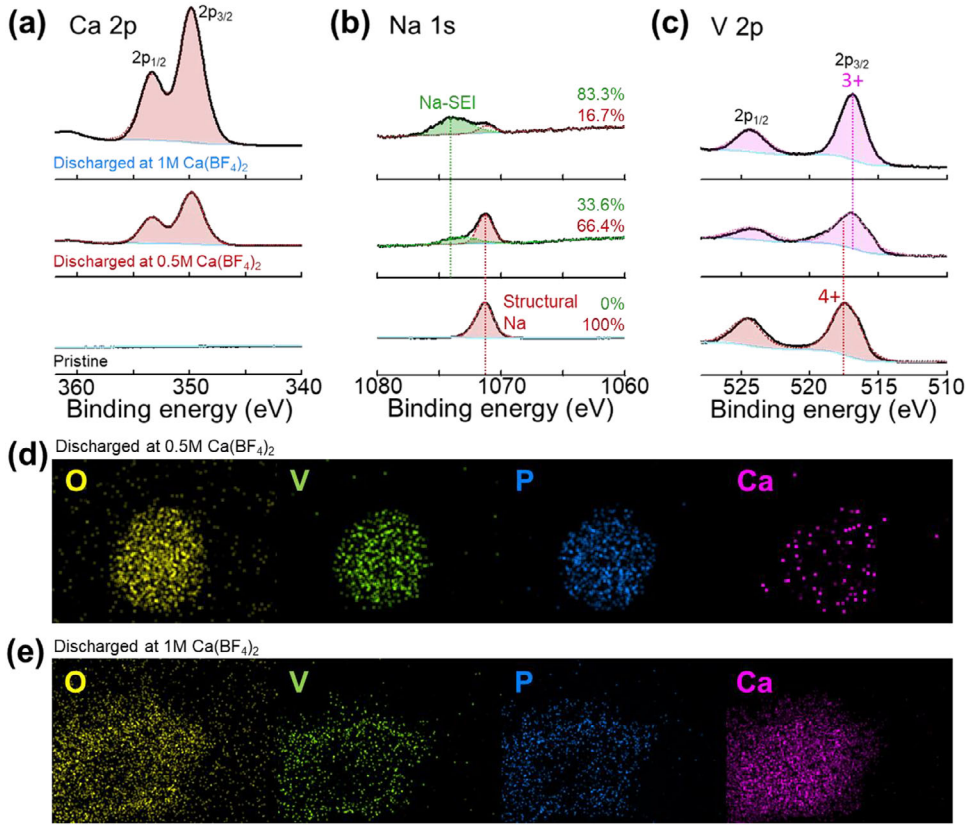

Figure 3. XPS spectra for a) Ca 2p, b) Na 1s and c) V 2p at pristine state and after discharged at 0.5 and 1 M $Ca(BF_4)_2$ in EC:PC (Vol/Vol = 1:1) electrolytes, TEM-EDX elemental mapping of $Na_1V_2(PO_4)_3$, after discharged electrodes at (d) 0.5 M and (e) 1 M $Ca(BF_4)_2$ in EC:PC (Vol/Vol = 1:1) electrolytes.

model and interpretation of the impedance responses are presented in Figure 2b, providing a detailed understanding of the influence of electrolyte concentration on resistance components and ion transport behavior.

Previous studies have shown that the $Na_1V_2(PO_4)_3$ structure requires several activation cycles for optimal performance.[37] Activation cycles conducted at 75 °C effectively enhanced the material's performance. While the theoretical capacity of $Na_1V_2(PO_4)_3$ is 130.8 mAh g^{-1}, previous reports have recorded capacities below ≈70 mAh g^{-1}.[37] To address this limitation, systematic activation studies were conducted. Galvanostatic discharge/charge testing at 75 °C (Figure 2c) revealed abnormally high charge capacities for the 0.5 M electrolyte, which were attributed to parasitic side reactions between the electrode and electrolyte—likely involving the formation of CaF_2 (Figure S4, Supporting Information).[37] This difference in side reactions may arise from variations in the Ca^{2+} solvation structure between the two electrolytes, particularly at elevated temperatures. At lower concentration (0.5 M), Ca^{2+} is predominantly coordinated with EC and PC molecules, forming more stable and isolated solvation shells. In contrast, the higher concentration (1.0 M) results in reduced availability of free solvent molecules, increasing the probability of contact ion pair (CIP) or solvent-shared ion pair (SSIP) formation. These ion aggregates tend to exhibit stronger electrostatic interactions, which can promote interfacial side reactions such as CaF_2 formation. Despite the presence of side reactions (increased R_{CEI} resistance) in the 1 M electrolyte, the system demonstrates improved electrochemical performance, attributed to more pronounced interfacial reactions (decreased R_{ct} resistance). In addition, while CEI composition may influence interfacial resistance, the overall performance difference appears to be more strongly governed by the structural activation of $NaV_2(PO_4)_3$, as evidenced by the rapid unit cell expansion and improved Ca^{2+} diffusion in the 1 M electrolyte (Figure 4a–c).

The differential capacity (dQ/dV) plots (Figure 2d) highlight improved oxidation-reduction reversibility in the 1 M $Ca(BF_4)_2$ electrolyte at 75 °C compared to the 0.5 M electrolyte. The 1 M electrolyte exhibits sharper and more distinct redox peaks, indicating stable and reversible calcium-ion insertion and extraction within the $Na_1V_2(PO_4)_3$ structure under elevated temperature conditions. The enhanced reversibility observed in the 1 M electrolyte can be ascribed to its optimized desolvation energy and more favorable charge transfer kinetics, which collectively mitigate polarization and facilitate efficient interfacial charge transport. Conversely, although the 0.5 M electrolyte exhibits higher ionic conductivity and lower CEI resistance, the presence of a smaller reduction peak indicates increased polarization and reduced redox efficiency. Following activation, the electrochemical performance at room temperature was evaluated (Figure 2e).

The cell activated with the 1 M electrolyte achieved a capacity of 106.9 mAh g^{-1}, whereas the cell activated with the 0.5 M electrolyte exhibited a lower capacity of 58.8 mAh g^{-1}. These results indicate that high-temperature activation using the 1 M

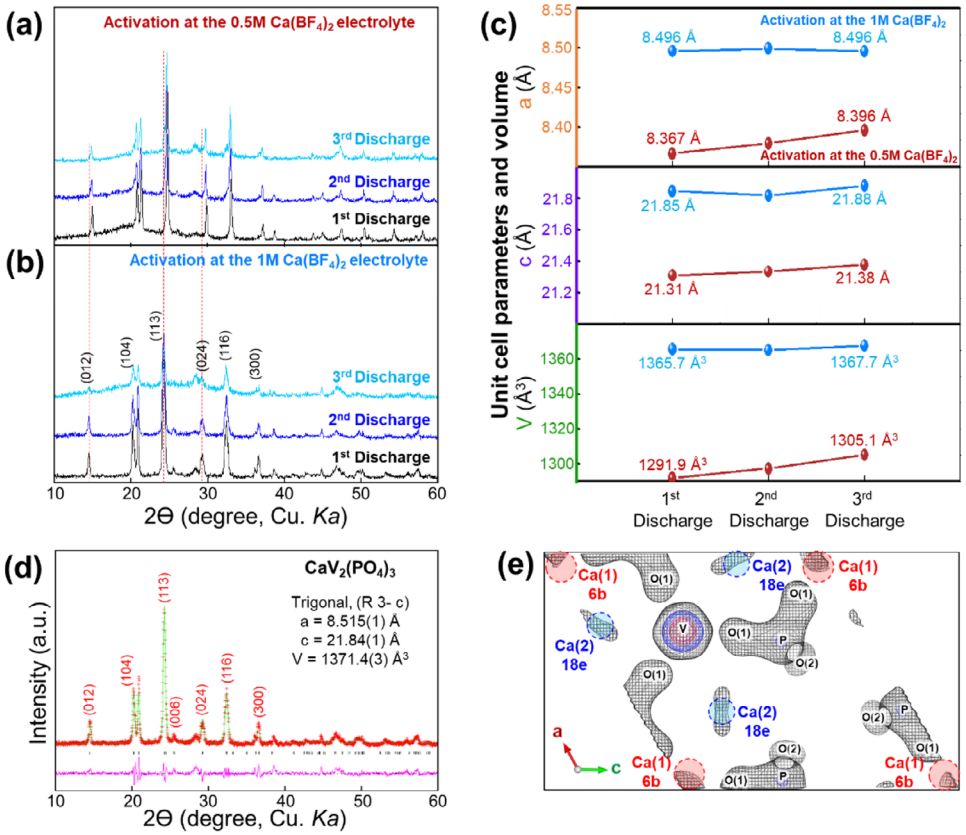

Figure 4. XRD patterns during the $Na_1V_2(PO_4)_3$ activation process in (a) 0.5 and (b) 1 M $Ca(BF_4)_2$ in EC:PC (Vol/Vol = 1:1) electrolytes, c) unit cell parameter and volumes changes during activation process at (red) 0.5 and (blue) 1 M $Ca(BF_4)_2$ in EC:PC (Vol/Vol = 1:1) electrolytes, d) Rietveld refinement result of $CaV_2(PO_4)_3$ (calcium activated and discharged state), e) Fourier electron density map of $CaV_2(PO_4)_3$.

$Ca(BF_4)_2$ in EC:PC (Vol/Vol = 1:1) electrolyte enhances room-temperature capacity by minimizing R_{ct} resistance, despite the presence of side reactions. (Figure 2f). Rate performance and cyclability at 25 °C were assessed after the high temperature activation (Figure 2g,h). The fully activated $Na_1V_2(PO_4)_3$ with the 1 M electrolyte demonstrated superior high-rate capabilities, delivering specific capacities of 101, 84.9, 67.3, and 4.2 mAh g^{-1} at current densities of 10, 20, 40, and 80 mA g^{-1}, respectively (Figure S6, Supporting Information). In comparison, the cell with the 0.5 M electrolyte showed significantly lower capacities of 52.8, 45.0, 29.3, and 2.6 mAh g^{-1} at the same current rates (Figure S7, Supporting Information). Cyclability at 40 mA g^{-1} is illustrated in Figure 2h. The 1 M electrolyte system maintained a higher capacity of ≈80 mAh g^{-1}, though it exhibited more pronounced capacity fading over 100 cycles (42% retention, Figures S8 and S9, Supporting Information). This capacity decay can be attributed to structural degradation from repeated Ca^{2+} insertion/extraction, as well as accumulation of interfacial byproducts such as CaF_2, which increase resistance and hinder ion transport during cycling. But, suffered from structural collapse due to active charge/discharge reactions even after few cycles (Figure 4b). Meanwhile, the 0.5 M electrolyte system exhibited a lower initial capacity (≈20 mAh g^{-1}), attributed to the inactive electrode and reduced diffusion kinetics. Notably, the use of $Ca(BF_4)_2$ as the electrolyte, which is more prone to CaF_2-related side reactions than other salts such as $Ca(TFSI)_2$, may also contribute to the faster capacity fading observed in this study. These results highlight the critical importance of electrolyte concentration and activation conditions in optimizing the electrochemical performance of $Na_1V_2(PO_4)_3$ for calcium-ion batteries. While direct quantification of Ca^{2+} diffusivity is limited in this study, future work will explore advanced techniques such as GITT or PITT to better evaluate ion transport properties.

2.3. Mechanism of Calcium Activation Process on $Na_1V_2(PO_4)_3$

Following the activation process with 0.5 and 1 M electrolytes, the electrode materials were analyzed using TEM-EDX and X-ray photoelectron spectroscopy (XPS). The XPS profiles of calcium 2p, sodium 1s, and vanadium 2p are presented in **Figure** 3a–c. Notably, the spectra in Figure 3a,c highlight prominent vanadium redox couples and an increase in calcium peaks. In addition, the calcium signals in the XPS profiles are significantly higher for the 1 M electrolyte compared to the 0.5 M electrolyte, indicating that the host structure reacts more extensively with the 1 M electrolyte (Figure 3a). Figure 3b also highlights the Na 1s signal. For $Na_1V_2(PO_4)_3$ and electrodes activated with the 0.5 M electrolyte, sodium peaks are still clearly visible, suggesting that sodium ions remain within the host structure, consistent with previous results.[37] However, when activated with the 1 M electrolyte, the sodium peak is nearly absent, indicating that sodium

ions in the pristine $Na_1V_2(PO_4)_3$ structure are almost completely replaced by calcium ions during the activation process. However, it appears that the formation of Na-containing CEI layers is more pronounced on the surface of the activated cathode material. Such separation of Na-related peaks has also been reported in previous studies.[38]

These results suggest a partial Na—Ca exchange, but bulk-level substitution, especially at the 6b site, cannot be confirmed without depth-resolved analysis. The V 2p spin-orbitals further confirm the role of vanadium as the redox center for calcium storage. The pristine $Na_1V_2(PO_4)_3$ structure exhibits distinct V 2p peaks in the 505–528 eV range, specifically at 517.5 eV (V^{4+} $2p_{3/2}$), 515.5 eV (V^{3+} $2p_{3/2}$), and 524.9 eV (V^{4+} $2p_{1/2}$). After discharge, these peaks shift to lower binding energy, providing direct evidence of the vanadium redox process during calcium-ion storage.

Figure 3d,e presents TEM-EDX elemental mapping of the electrode materials in $Na_1V_2(PO_4)_3$, and after activation with 0.5 and 1 M $Ca(BF_4)_2$ in EC:PC (Vol/Vol = 1:1) electrolytes. Based on EDX mapping analysis, the elemental distribution in the 0.5 M electrolyte is relatively uniform across the sample, whereas in the 1.0 M electrolyte, the distribution is less homogeneous. The signal intensities of O, V, and P are notably reduced toward the central region of the sample; however, the Ca signal remains relatively strong in these areas. This observation suggests that, in the high-concentration electrolyte, accelerated interfacial side reactions contribute to the detection of Ca not only from intercalated species but also from surface reaction byproducts. Also, sodium atoms are absent in the activated samples 1 M electrolyte. These findings align well with the XPS results, confirming successful ion exchange and uniform calcium incorporation into the activated electrode materials. However, we acknowledge that the strong calcium signal may also include contributions from CEI species formed on the surface. Distinguishing between bulk intercalation and surface deposition would require depth-resolved techniques such as XPS etching or TOF-SIMS, which are currently beyond the scope of this study but are planned for future work.

Electrodes activated with the 1 M electrolyte exhibited a diminished sodium signal compared to those treated with the 0.5 M electrolyte, suggesting more complete exchange and activation of sodium ions in the $Na_1V_2(PO_4)_3$ structure with calcium ions. However, due to the solubility limit of $Ca(BF_4)_2$ (≈1.0 M), further Ca incorporation may require alternative approaches such as electrolyte additives or sequential activation protocols. The stable cycling performance indicates that calcium ions, not sodium, act as the main charge carriers after activation, as residual Na^+ is likely diluted into the electrolyte and does not participate in subsequent reactions.

To clarify the activation mechanism, we emphasize that the formation of $Ca_1V_2(PO_4)_3$ does not proceed through a fully desodiated intermediate phase such as $V_2(PO_4)_3$, which is generally challenging to isolate due to its structural instability. Instead, XPS analysis of the discharged state (Figure 3b), combined with EDX mapping during discharge in a Ca metal cell (Figure S4, Supporting Information), reveals negligible sodium content, indicating that calcium ions directly replace sodium ions via a Ca—Na ion-exchange mechanism during the activation process. In particular, after discharge, the EDX line-scan data reveal that calcium participates in the overall reaction but is especially enriched at the surface (Figure S5, Supporting Information). Additionally, we analyzed the structural changes occurring during the activation process in each electrolyte, as shown in Figure 4 below.

To investigate the structural activation mechanism of $Na_1V_2(PO_4)_3$, we conducted XRD analyses (**Figure 4a–c**). Figure 4a,b XRD patterns of the activation process in a 0.5 and 1 M $Ca(BF_4)_2$ in EC:PC (Vol/Vol = 1:1) electrolyte, which shows the first, second, and third discharged states of the electrodes. In the 0.5 M electrolyte, the unit cell parameters gradually increased with each cycle, indicating an incremental activation process. In contrast, activation in the 1 M electrolyte resulted in a fully activated structure within the first cycle, evidenced by an immediate and significant expansion of the unit cell parameters. Figure 4c presents the detailed XRD analysis of the unit cell parameters. For the 0.5 M electrolyte, the unit cell parameter a gradually increased from 8.367 to 8.396 Å, c from 21.31 to 21.38 Å, and the unit cell volume from 1291.9 to 1305.1 $Å^3$ over multiple cycles. On the other hand, in the 1 M electrolyte, the unit cell parameter a reached 8.496 Å, c = 21.85 Å, and the unit cell volume 1365.7 $Å^3$ at the first cycle, maintaining these values in subsequent cycles. The rapid and complete activation in the 1 M electrolyte minimizes the number of cycles required for full activation, whereas the gradual activation in the 0.5 M electrolyte suggests the need for tens of cycles. These differences in unit cell volume also influence calcium-ion diffusion pathways, with the 0.5 M system likely experiencing higher diffusion barriers due to incomplete structural adaptation. Similar to strategies developed for lithium-based batteries, surface doping and carbon-based compositing techniques may also be employed to further activate and stabilize the cathode material structure.[39–41]

To further understand the calcium-incorporated structure activated in the 1 M electrolyte, we performed Rietveld refinement in Figure 4d. The discharged structure retained its NASICON-type trigonal crystal structure within the R $\bar{3}$ c space group, with refined lattice parameters of a = 8.515(1) Å and c = 21.84(1) Å. Detailed crystallographic information is provided in Table S3 (Supporting Information).

We also analyzed the calcium positions within the structural framework using a Fourier electron density map (Figure 4e). The results indicate that Ca^{2+} predominantly occupies the 6b site, a spacious coordination site, while a small fraction is distributed at the 18e site. The electron density map clearly reveals the presence of an electron cloud at these sites, and the ICP results (Table S4, Supporting Information) further suggest that sodium ions are almost completely removed, indirectly supporting the conclusion that the residual Na^+ at the 18e site has been exchanged with Ca^{2+}. However, more precise confirmation will require post-mortem analyses in future studies.

It is worth noting that our previous study explored chemical desodiation of $Na_3V_2(PO_4)_3$ using NO_2BF_4 and reported limited activation, as the third Na^+ ion at the 6b site remained immobile.[37] In contrast, the present study demonstrates that electrochemical activation at elevated temperature (75 °C), particularly in 1 M $Ca(BF_4)_2$ electrolyte, promotes thermally assisted Na^+/Ca^{2+} ion-exchange, resulting in near-complete Na removal and superior calcium storage performance. This mechanistic difference highlights the critical role of electrochemical activation conditions in enabling Na mobility, which could not be achieved by chemical oxidation alone. The current work thus expands upon our

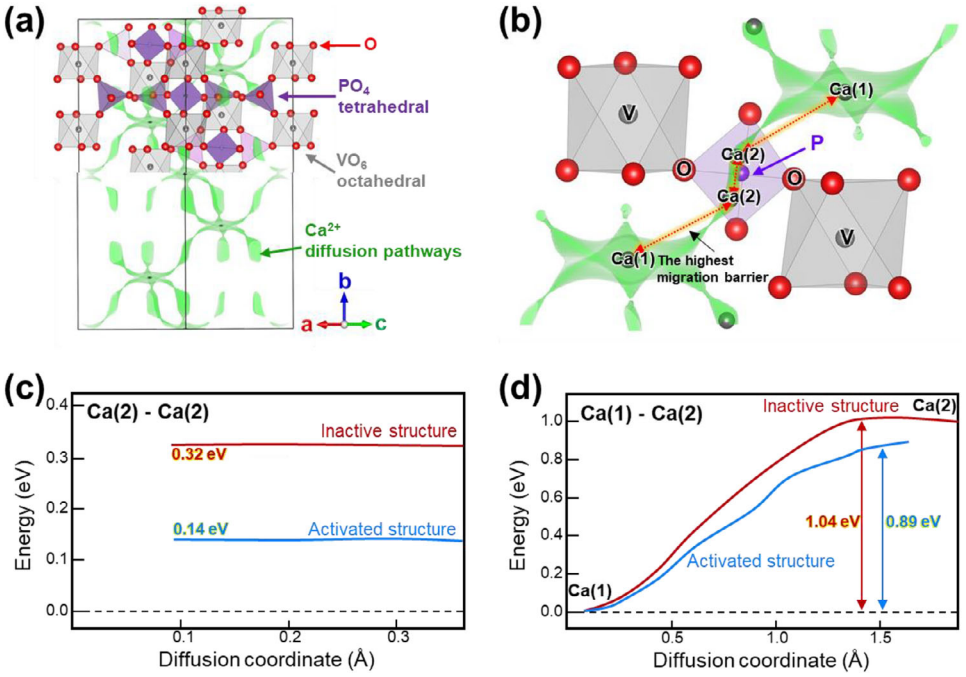

Figure 5. Calculated calcium migration barriers and paths into NVP crystal structure a) unit cell view, b) local diffusion pathway, two step migration barriers c) Ca(2)—Ca(2) d) Ca(1)—Ca(2) site.

previous findings, providing new insight into ion exchange dynamics and interfacial effects in NASICON-type Ca-ion cathodes.

The calcium migration pathways and energy barriers were calculated using the soft BV-GUI program,[42] as shown in **Figure 5**. The structural models were constructed based on the unit cell parameters of the activated lattices obtained from each electrolyte. The presence of Na within the framework was excluded from the diffusion pathway calculations, as residual Na ions could act as blocking species for Ca^{2+} migration. Consequently, the diffusivity of Ca^{2+} was evaluated using the activated unit cell parameters and the $V_2(PO_4)_3$ framework.

The possible three-dimensional calcium migration pathways within the NASICON structure, consisting of PO_4 tetrahedra and VO_6 octahedra, are depicted in Figure 5a. Figure 5b provides a detailed view of the local diffusion pathways. When calcium is inserted into the structure, the most stable site is the Ca(1) site. For calcium ions to diffuse from one Ca(1) site to another, they must pass through the intermediate Ca(2) site, which requires overcoming a high energy barrier. To clearly understand, the diffusion barriers were characterized based using the unit cell parameters of the structures activated in 0.5 and 1 M electrolytes. For convenience, the structure activated in 0.5 M electrolyte is referred to as the "inactive structure," while the structure activated in 1 M electrolyte is referred to as the "activated structure." Figure 5c shows the calculated minor diffusion barriers between Ca(2)—Ca(2) sites. The energy differences in the balanced state were 0.32 eV for the inactive structure and 0.14 eV for the activated structure. However, the diffusion barriers for Ca(2)—Ca(2) migration were negligible in both cases, indicating that this pathway has little impact on the overall calcium diffusion process. The most critical pathway involves calcium migration from the Ca(1) site to the Ca(2) site, where the highest activation barriers are observed (Figure 5d). For the inactive structure, the energy barrier was calculated to be 1.04 eV, whereas the activated structure exhibited a lower barrier of 0.89 eV. This reduction in the activation barrier demonstrates that the structure activated in 1 M $Ca(BF_4)_2$ in EC:PC (Vol/Vol = 1:1) electrolytes enables faster calcium-ion diffusion within the framework. This enhanced diffusion capability significantly boosts the electrochemical performance of the activated structure, contributing to improved rate capabilities and overall battery efficiency. While the calculated calcium migration barriers based on the BVS approach offer valuable insights into structural activation effects, it is important to note that these calculations were performed assuming a fully Ca-substituted framework. Experimental data (e.g., XPS and EDX) indicate that residual Na^+ may still be present, particularly in partially activated structures. Incorporating mixed Na^+/Ca^{2+} occupancy in future simulations will be crucial for more accurately capturing the real diffusion environment within the NASICON lattice.

The electrochemical performance of NVP has predominantly been assessed using activated carbon as the counter electrode, enabling the investigation of its intrinsic redox behavior without interference from an unstable anode. This strategy circumvents the limitations posed by calcium metal anodes, which often introduce complications due to their poor reversibility and surface instability. Specifically, the formation of passivation layers on the calcium surface significantly impedes reversible calcium plating and stripping,[7] frequently leading to cell failure and masking the true electrochemical characteristics of the cathode.

To directly probe the redox properties of NVP, a three-electrode configuration was employed using an electrolyte composed of 0.5 M $Ca(BF_4)_2$ in EC:PC (Vol/Vol = 1:1), supplemented with

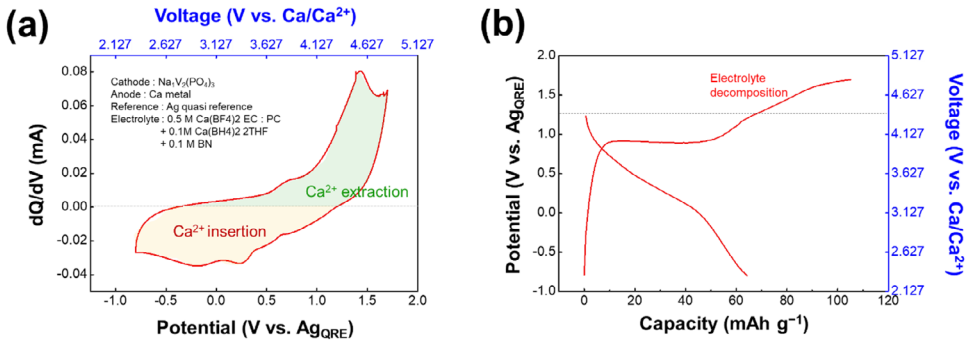

Figure 6. a) CV profile and b) galvanostatic charge discharge curve under 20 mA g^{-1} current of Ca metal/0.5 M $Ca(BF_4)_2$ in EC:PC (Vol/Vol = 1:1)/$Na_1V_2(PO_4)_3$ cell.

0.1 M $Ca(BH_4)_2$·2THF and 0.1 M Boron Nitride (BN) as functional additives. As shown in **Figure 6a**, well-defined oxidation and reduction peaks were observed, indicating reversible redox activity centered ≈3.5 V vs Ca/Ca^{2+} (Figure S10, Supporting Information). Complementary galvanostatic charge–discharge experiments (Figure 6b) revealed consistent behavior, delivering a discharge capacity of ≈65 mAh g^{-1} at a current density of 20 mA g^{-1}. However, electrolyte decomposition and side reactions became prominent above 4.3 V vs Ca/Ca^{2+}, suggesting this as the upper voltage limit for stable operation. Notably, the charge profiles exhibited sharp and distinct plateaus, whereas the discharge profiles were comparatively sluggish.

This asymmetry is likely attributed to the substantial desolvation energy barrier associated with Ca^{2+} ions during discharge, underscoring the importance of desolvation kinetics in governing the overall electrochemical performance of calcium-based battery systems. These findings highlight a critical area for further research in the pursuit of high-efficiency calcium-ion technologies.

3. Conclusion

In conclusion, this study elucidates the activation mechanism enabling efficient calcium-ion storage within the NASICON-$NaV_2(PO_4)_3$ structure, establishing it as a promising cathode material for CIBs at ambient temperatures. Activation in high-concentration electrolytes was shown to significantly enhance performance. The material exhibited an impressive reversible discharge capacity of 106.9 mAh g^{-1} at a current of 10 mA g^{-1}, reflecting an 82% improvement compared to its pristine state, while maintaining a stable average voltage of 3.5 V (vs Ca/Ca^{2+}) and notable cyclability in nonaqueous electrolytes. The activation process was optimized using 1 M $Ca(BF_4)_2$ in EC:PC (Vol/Vol = 1:1) electrolyte, outperforming the 0.5 M counterpart. Advanced structural and elemental analyses via XPS, and TEM mapping confirmed the complete exchange of residual sodium ions with calcium within the $NaV_2(PO_4)_3$ framework. This enhanced ion exchange effect, facilitated by the stability of the high-concentration electrolyte during oxidation reactions, likely arises from structural transformations induced by activation. The enlarged unit cell parameters and volume in the activated structure further promote improved calcium-ion diffusion pathways. Notably, the complete substitution of sodium with calcium resulted in a reduced ion diffusion barrier, lowering it from 1.04 to 0.89 eV. This reduction significantly accelerates calcium-ion diffusion and enables robust operation at ambient temperatures.

These findings provide valuable insights into the design and development of advanced oxide-based materials, highlighting the critical role of electrolyte optimization and structural activation in achieving high-performance cathodes for nonaqueous calcium-ion batteries.

4. Experimental Section

Material Synthesis and Characterization of $Na_3V_2(PO_4)_3$: Carbon-coated $Na_3V_2(PO_4)_3$ was prepared using the sol–gel technique.[37] Initially, high-purity chemicals—sodium carbonate (Na_2CO_3, > 99.5% from Sigma–Aldrich), vanadium pentoxide (V_2O_5, > 99.6% from Alfa Aesar), ammonium phosphate ($(NH_4)_2HPO_4$, > 98% from Sigma–Aldrich), and oxalic acid (98% purity, also from Sigma–Aldrich)—were thoroughly dissolved in 100 mL deionized water. This solution was then dried at a temperature of 80 °C for one day. The resulting dried mixture was baked at a temperature of 850 °C for 8 h within a tube furnace, under a controlled hydrogen (H_2) atmosphere. To analyze the morphology of the produced powder, a TEM (model Themis Z) equipped with an EDX system was employed.

Electrochemical Characterization: All electrochemical tests were conducted using homemade three-electrode cells (swagelok type). The composition of the working electrodes was a mix of $Na_3V_2(PO_4)_3$ powder, Super P conducted carbon from Timcal Graphite and Carbon, and a binder of poly(vinylidene)fluoride (PVDF) from Kureha Co., in a ratio of 8:1:1 by weight. This mixture was homogenized in NMP (N-methyl-2-pyrrolidone, Sigma–aldrich) before being spread onto a 16 µm thick aluminium substrate supplied by Wellcos Co. After an overnight drying process at 70 °C, the electrodes were compacted using a press. For the counter and reference electrodes, activate carbon pellet was chosen, separated by glass fiber paper from Whatman, and the electrolyte solution was made of 0.5 and 1 M $Ca(BF_4)_2$ in a EC:PC (Vol/Vol = 1:1) mixture solvent. The electrolyte solution was dried overnight at ≈120 °C on a hotplate within a glove box to eliminate residual moisture. Subsequently, a syringe filter was employed to remove any precipitated solids. When the concentration exceeded 1.0 M, the solution reached saturation, preventing further dissolution of the salt.

Diffusion Barrier Calculation: Regarding the calculation of diffusion barriers, the soft BV-GUI program (v131)[43,44] was utilized to determine cation migration barriers, relying on the unit cell parameter for the non-activated structure (0.5 M activated unit cell) and activated structure (1 M activated unit cell) using XRD analyses using GSAS.[45] Visualization of the 3D diffusion paths was achieved using the VESTA software, version 3.[46]

Supporting Information

Supporting Information is available from the Wiley Online Library or from the author.

Acknowledgements

This work was supported by Pukyong National University. Also supported by the National Research Foundation of Korea (NRF) grant funded by the Korean government (MSIT) (grant no. 2020R1A2C2007070).

Conflict of Interest

The authors declare no conflict of interest.

Data Availability Statement

The data that support the findings of this study are available in the supplementary material of this article.

Keywords

Ca^{2+} intercalation, Ca-ion batteries, cathode material, $NaV_2(PO_4)_3$, non-aqueous electrolyte

Received: June 17, 2025
Revised: September 26, 2025
Published online: October 8, 2025

[1] J. W. Choi, D. Aurbach, *Nat. Rev. Mater.* **2016**, *1*, 16013.
[2] Y. Liang, H. Dong, D. Aurbach, Y. Yao, *Nat. Energy* **2020**, *5*, 646.
[3] Y. Wang, R. Chen, T. Chen, H. Lv, G. Zhu, L. Ma, C. Wang, Z. Jin, J. Liu, *Energy Storage Mater.* **2016**, *4*, 103.
[4] H. Bu, H. Lee, D. Setiawan, S.-T. Hong, *Chem. Phys. Rev.* **2022**, *3*, 011309.
[5] Y. Yang, X. Xiong, J. Chen, X. Peng, D. Chen, F. Pan, *J. Magnes. Alloy.* **2023**, *11*, 2611.
[6] D. Setiawan, H. Lee, J. Pyun, A. Nimkar, N. Shpigel, D. Sharon, S.-T. Hong, D. Aurbach, M. S. Chae, *J. Magnes. Alloy.* **2024**, *12*, 3476.
[7] A. Ponrouch, C. Frontera, F. Bardé, M. R. Palacín, *Nat. Mater.* **2016**, *15*, 169.
[8] J. Forero-Saboya, C. Bodin, A. Ponrouch, *Electrochem. Commun.* **2021**, *124*, 106936.
[9] Z. Zhao-Karger, Y. Xiu, Z. Li, A. Reupert, T. Smok, M. Fichtner, *Nat. Commun.* **2022**, *13*, 3849.
[10] S. J. R. Prabakar, A. B. Ikhe, W. B. Park, K. Chung, H. Park, K. Kim, D. Ahn, J. S. Kwak, K. Sohn, M. Pyo, *Adv. Sci.* **2019**, *6*, 1902129.
[11] J. Zhang, Z. Chang, Z. Zhang, A. Du, S. Dong, Z. Li, G. Li, G. Cui, *ACS Nano* **2021**, *15*, 15594.
[12] J. Muldoon, C. B. Bucur, T. Gregory, *Chem. Rev.* **2014**, *114*, 11683.
[13] J. Forero-Saboya, C. Davoisne, R. Dedryvère, I. Yousef, P. Canepa, A. Ponrouch, *Energy Environ. Sci.* **2020**, *13*, 3423.
[14] Y. Zhao, A. Wang, L. Ren, X. Liu, J. Luo, *J. Energy Chem.* **2022**, *70*, 174.
[15] M. H. Alfaruqi, S. Lee, H. Kang, B. Sambandam, V. Mathew, J.-Y. Hwang, J. Kim, *J. Phys. Chem. C* **2022**, *126*, 9209.
[16] Z. Zhang, X. Zhang, X. Zhao, S. Yao, A. Chen, Z. Zhou, *ACS Omega* **2019**, *4*, 7822.
[17] R. Verrelli, A. P. Black, C. Pattanathummasid, D. S. Tchitchekova, A. Ponrouch, J. Oró-Solé, C. Frontera, F. Bardé, P. Rozier, M. R. Palacín, *J. Power Sources* **2018**, *407*, 162.
[18] H. Bu, H. Lee, J. Hyoung, J. W. Heo, D. Kim, Y. J. Lee, S.-T. Hong, *Chem. Mater.* **2023**, *35*, 7974.
[19] T. N. Vo, H. Kim, J. Hur, W. Choi, I. T. Kim, *J. Mater. Chem. A* **2018**, *6*, 22645.
[20] T. Tojo, H. Tawa, N. Oshida, R. Inada, Y. Sakurai, *J. Electroanal. Chem.* **2018**, *825*, 51.
[21] M. Cabello, F. Nacimiento, R. Alcántara, P. Lavela, C. P. Vicente, J. L. Tirado, *Chem. Mater.* **2018**, *30*, 5853.
[22] M. S. Chae, H. H. Kwak, S.-T. Hong, *ACS Appl. Energy Mater.* **2020**, *3*, 5107.
[23] M. Cabello, F. Nacimiento, J. R. González, G. Ortiz, R. Alcántara, P. Lavela, C. Pérez-Vicente, J. L. Tirado, *Electrochem. Commun.* **2016**, *67*, 59.
[24] D. S. Tchitchekova, A. Ponrouch, R. Verrelli, T. Broux, C. Frontera, A. Sorrentino, F. Bardé, N. Biskup, M. E. A. Dompablo, M. R. Palacín, *Chem. Mater.* **2018**, *30*, 847.
[25] C. Lee, Y.-T. Jeong, P. M. Nogales, H.-Y. Song, Y. Kim, R.-Z. Yin, S.-K. Jeong, *Electrochem. Commun.* **2019**, *98*, 115.
[26] R. Verrelli, A. Black, R. Dugas, D. Tchitchekova, A. Ponrouch, M. R. Palacin, *J. Electrochem. Soc.* **2020**, *167*, 070532.
[27] A. L. Lipson, S. Kim, B. Pan, C. Liao, T. T. Fister, B. J. Ingram, *J. Power Sources* **2017**, *369*, 133.
[28] M. S. Chae, D. Setiawan, H. J. Kim, S.-T. Hong, *Batteries* **2021**, *7*, 54.
[29] X. Xu, M. Duan, Y. Yue, Q. Li, X. Zhang, L. Wu, P. Wu, B. Song, L. Mai, *ACS Energy Lett.* **2019**, *4*, 1328.
[30] M. S. Chae, A. Nimkar, N. Shpigel, Y. Gofer, D. Aurbach, *ACS Energy Lett.* **2021**, *6*, 2659.
[31] A. L. Lipson, S.-D. Han, S. Kim, B. Pan, N. Sa, C. Liao, T. T. Fister, A. K. Burrell, J. T. Vaughey, B. J. Ingram, *J. Power Sources* **2016**, *325*, 646.
[32] P. Padigi, G. Goncher, D. Evans, R. Solanki, *J. Power Sources* **2015**, *273*, 460.
[33] N. Kuperman, P. Padigi, G. Goncher, D. Evans, J. Thiebes, R. Solanki, *J. Power Sources* **2017**, *342*, 414.
[34] A. L. Lipson, B. Pan, S. H. Lapidus, C. Liao, J. T. Vaughey, B. J. Ingram, *Chem. Mater.* **2015**, *27*, 8442.
[35] T. Tojo, Y. Sugiura, R. Inada, Y. Sakurai, *Electrochim. Acta* **2016**, *207*, 22.
[36] T. N. Vo, J. E. Kang, H. Lee, S. Lee, S. Ahn, J. Hur, I. T. Kim, *EcoMat* **2023**, *5*, 12285.
[37] B. Jeon, J. W. Heo, J. Hyoung, H. H. Kwak, D. M. Lee, S.-T. Hong, *Chem. Mater.* **2020**, *32*, 8772.
[38] S. Ivanova, E. Zhecheva, R. Kukeva, D. Nihtianova, L. Mihaylov, G. Atanasova, R. Stoyanova, *ACS Appl. Mater Inter.* **2016**, *8*, 17321.
[39] L. Li, R. Wu, H. Ma, B. Cheng, S. Rao, S. Lin, C. Xu, L. Li, Y. Ding, L. Mai, *Small* **2023**, *19*, 2300762.
[40] S. Rao, R. Wu, Z. Zhu, J. Wu, Y. Ding, L. Mai, *Nano Energy* **2023**, *112*, 108462.
[41] K. Wang, Y. Wang, J. Wang, H. Wang, C. Ding, Z. Zheng, Y. Liu, Z. Luo, Y. Ding, *Adv. Funct. Mater.* **2025**, *35*, 2422689.
[42] H. Chen, L. L. Wong, S. Adams, *Acta Crystallogr. Sect. B: Struct. Sci., Cryst. Eng. Mater.* **2019**, *75*, 18.
[43] P. W. Ruch, D. Cericola, M. Hahn, R. Kötz, A. Wokaun, *J. Electroanal. Chem.* **2009**, *636*, 128.
[44] L. L. Wong, K. C. Phuah, R. Dai, H. Chen, W. S. Chew, S. Adams, *Chem. Mater.* **2021**, *33*, 625.
[45] B. H. Toby, *J. Appl. Crystallogr.* **2001**, *34*, 210.
[46] K. Momma, F. Izumi, *J. Appl. Crystallogr.* **2011**, *44*, 1272.